2022-23 Technical Design Report

Cal Aero SAE

Team 015

University of California, Berkeley



Team Members:

Jesus Carpio, Upasana Dilip, Luke Fewx, Arya Gandhi, Angel Hernandez, Franco Huemura, Sohan Jayanth, Valeria Jimenez, Pratik Jitendra, Linda Krellner, Dylan Lee, Ethan Long, Stephanie Loo, Rafael Petrosian, Jude Russel, Diego Sandoval, Kamron Soltani, Tam Tran, Tyler Vo, Richie Woo

APPENDIX A - STATEMENT OF COMPLIANCE

Certification of Qualification

Team Name	Cal Aero SAE	Team Number	015
School	UC Berkeley		
Faculty Advisor	Omer Savas		
Faculty Advisor's Email	savas@berkeley.edu		

Statement of Compliance

As faculty Adviser:

OS (Initial) I certify that the registered team members are enrolled in collegiate courses.

OS (Initial) I certify that this team has designed and constructed the radio-controlled aircraft in the past nine (9) months with the intention to use this aircraft in the **2024** SAE Aero Design competition, without direct assistance from professional engineers, R/C model experts, and/or related professionals.

OS (Initial) I certify that this year's Design Report has original content written by members of this year's team.

OS (Initial) I certify that all reused content have been properly referenced and is in compliance with the University's plagiarism and reuse policies.

OS (Initial) I certify that the team has used the Aero Design inspection checklist to inspect their aircraft before arrival at Technical Inspection and that the team will present this completed checklist, signed by the Faculty Advisor or Team Captain, to the inspectors before Technical Inspection begins.

Omer Savas	March 1·2024
Signature of Faculty Advisor	Date
	03/01/2024
Signature of Team Captain	Date

Note: **A copy of this statement needs to be included in your Design Report as page 2 (Reference Section 4.3)**

Table of Contents

Cover Page 1

Statement of Compliance 2

Table of Contents 3

Table of Figures 4

Table of Tables 4

1 Executive Summary 5
- 1.1 System Overview . . . 5
- 1.2 Competition Projections . . . 5
- 1.3 Discriminators . . . 5

2 Scheduling, Budget, and Risk 6

3 Overall Design and Configuration 7
- 3.1 Overall Vehicle Configuration . . . 7
- 3.2 Optimization . . . 7
  - 3.2.1 Airfoil Selection . . . 7
  - 3.2.2 Payload and Scoring Optimization . . . 8
  - 3.2.3 Design Sensitivities . . . 9

4 Load Derivations and Assumptions 10
- 4.1 Aerodynamic Loads . . . 10
  - 4.1.1 3-D Drag Considerations . . . 11
- 4.2 Landing Loads . . . 12

5 Structural Design and Analysis 12
- 5.1 Component Loading and Design . . . 12
  - 5.1.1 Classical Statics . . . 13
  - 5.1.2 Finite Element Analyses . . . 14
- 5.2 Landing Gear Configuration and Selection . . . 15
  - 5.2.1 Front Landing Gear . . . 16
  - 5.2.2 Rear Landing Gear . . . 16
- 5.3 Integration and Modularity Design . . . 18
  - 5.3.1 Tail to Fuselage Integration . . . 18
  - 5.3.2 Internal Tail Integration . . . 18
  - 5.3.3 Spar Integration . . . 19
- 5.4 Weight and Balance . . . 19

6 Aerodynamic Performance Analysis 19
- 6.1 Takeoff and Climb . . . 19
- 6.2 Lifting and Cruise Performance . . . 20
- 6.3 Stability . . . 21
  - 6.3.1 Horizontal Stabilizer . . . 21
  - 6.3.2 Vertical Stabilizer . . . 21
  - 6.3.3 Dynamic Stability Modes . . . 22
- 6.4 Control and Maneuverability . . . 23
  - 6.4.1 Elevators and Rudder . . . 23
  - 6.4.2 Ailerons . . . 24

7 Propulsion and Testing 24

8 Materials and Manufacturing **26**
8.1 Material Selection . . . 26
8.2 Manufacturing Technique Highlights . . . 26
8.2.1 Hollowfoils . . . 27
8.2.2 Wing Mount and Welds/Cold Welds . . . 27

9 Conclusion **28**

2D Drawing **29**

Table of Acronyms **30**

Table of Figures

1 Complete CAD of Aircraft (internal structures shown) . . . 5
2 2023-24 Season Schedule . . . 6
3 Score Optimization Plot (Score vs. Wingspan vs. Wing Area) for DAE-31 Airfoil . . . 9
4 Sensitivities of W_{payload} and Score to Fixed Parameters . . . 10
5 3D Drag simulation in XFLR5 . . . 11
6 Simulink Model for Landing Loads . . . 12
7 Example of Beam Analysis . . . 14
8 FEA of Wing Mount Truss . . . 14
9 FEA of Boom Tail and Wing Spar . . . 15
10 FLG CAD . . . 16
11 Topology Optimization for Aluminum RLG . . . 17
12 RLG Testing Setup . . . 17
13 Tail Integration Design . . . 18
14 Climb Analysis . . . 20
15 V-n Diagram for Vehicle . . . 20
16 Effectiveness Parameter Graph . . . 23
17 Static Thrust Testing Setup . . . 25
18 Calibrated Dynamic Thrust Models . . . 25
19 Hollowfoils and Testing . . . 27
20 Cold Weld Epoxy Testing . . . 28

Table of Tables

1 2023-24 Season Budget . . . 6
2 Safety Factors of Critical Components . . . 13
3 Critical Landing Gear Dimensions . . . 16
4 RLG Testing Deflections . . . 17
5 Weight and Balance Table . . . 19
6 Vertical Stabilizer Features and Sizing . . . 22
7 Thrust in Newtons for Various Motor/Propeller Combinations . . . 25
8 Cold Weld Adhesive Testing Results . . . 28

1 Executive Summary

1.1 System Overview

UC Berkeley's Aerospace SAE Team (015) presents an aircraft we believe is competitive at SAE Aero Design West. In the design of our aircraft, we utilized a combination of analytical calculations, simulation software, and physical testing. A complete Computer Aided Design (CAD) of the aircraft is shown in Fig. 1.

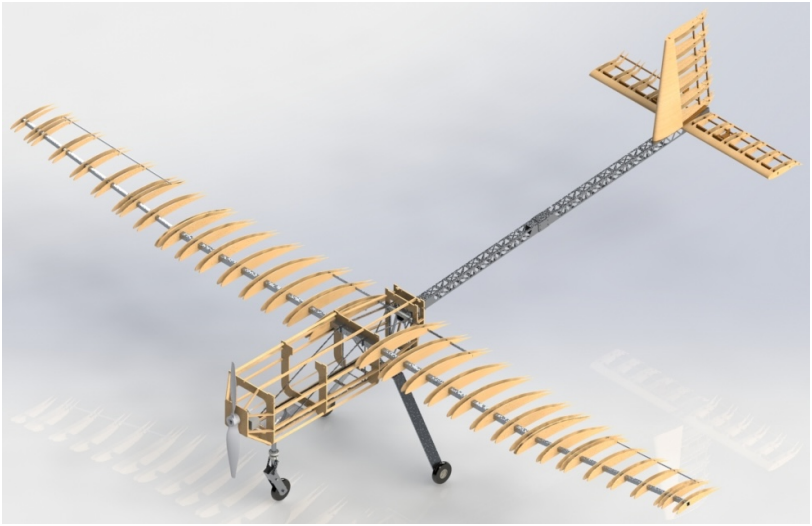


Figure 1: Complete CAD of Aircraft (internal structures shown)

1.2 Competition Projections

The overall objective of the competition is to carry as much payload as possible while overcoming the challenge of a modular vehicle design (no component can measure more than 48 inches along any primary axis). Last year, our aircraft had insufficient thrust to safely take off in the allotted 100-ft runway and inadequate structural integrity to survive the resulting crash. This year, we designed our aircraft to prioritize at least one successful scoring flight with minimal payload. Our cargo bay is positioned such that stability is maintained with any additional payload up to our maximum takeoff weight (MTOW), which carries 12lbf of payload. With a 15ft wingspan, we calculate [1] a maximum mission score of 49 points, which when compared to last year's scores, we believe to be sufficient for a high competition ranking. For more details regarding score optimization, see Sec. 3.2.2.

1.3 Discriminators

Besides being competitive, our aircraft also features several unique components. Several of these features re-imagine the competition's modularity challenge as an opportunity. For example, we implemented a polyhedral wing by angling the wing tip sections, and a raised tailplane by angling our boom tail. Additionally, in favor of reducing weight, our team explored a trailing link front landing gear, as well as cutouts in our boom tail to form a truss structure. Finally, we implemented washout and a slight forward sweep in our wing to increase stability and performance.

2 Scheduling, Budget, and Risk

Fig. 2 shows the overall schedule for our team this year, and Tab. 1 shows the overall budget for our team this year, including projected costs.

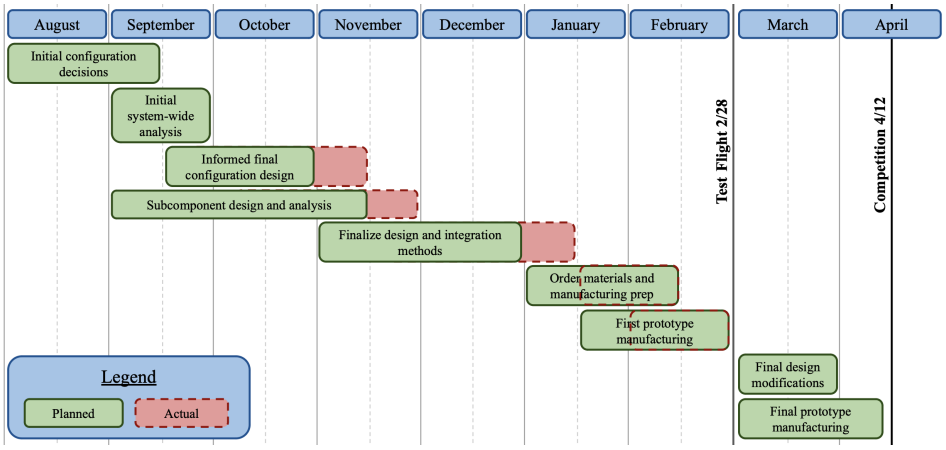


Figure 2: 2023-24 Season Schedule

Table 1: 2023-24 Season Budget

MATERIALS		**TRAVEL**		**LOGISTICS**	
Description	**Amount**	**Description**	**Amount**	**Description**	**Amount**
Balsa Wood	$861.86	Airbnb	$1995.39	Comp. Registration	$1500.00
Spruce Wood	$236.41	Gasoline (Projected)	$600.00	Club Maker Passes	$1250.00
Hardware	$323.98	U'Haul (Projected)	$1750.00	Polo Shirts	$550.00
Aluminum	$242.64	Supplies (Projected)	$1500.00		
Landing Gear	$187.00				
Remaining Materials	$500.00				
Materials Total	$2351.89	**Travel Total**	$6850.00	**Logistics Total**	$3300.00
Total Projected Spending: $12,501.89					

Operationally, our primary goal was to mitigate the unexpected roadblocks we encountered last year. These included: (1) Delays due to subcomponent dependencies, (2) Delays due to material availability, and (3) Extremely short time span to construct competition prototype. This year, we treated the above three challenges as risks, which we mitigated as follows.

1. In order to minimize delays due to the design of certain subcomponents depending on that of other subcomponents, we designed each component parametrically, allowing some dimensions and fastener locations to be modified if needed. Then, as we finalized our configuration, these dimensions were fixed. Additionally, the team members working on various subcomponents regularly met to facilitate any necessary communication.

2. Our strategies to mitigate delays due to material availability, or the lack thereof, were twofold. First, as seen in Fig. 2, we planned to order materials with plenty of time to spare for the competition. Because of this strategy, even though we were approximately 2 weeks behind schedule, we still managed to obtain all necessary materials in time. Second, we designed for material parsimony as much as possible. In other words, reused as many

materials from previous competition seasons as possible and designed to use the same parts (i.e. fasteners) across various subcomponents if possible.

3. Last competition season, our team scheduled a late test flight (in mid-late March) for our prototype. This resulted in very little time to make final design modifications and construct our final protoytpe. This year, in order to mitigate the risk of insufficient time to construct our final prototype, we scheduled a test flight for February and aggressively worked towards achieving this goal.

3 Overall Design and Configuration

3.1 Overall Vehicle Configuration

Our vehicle will have a wingspan b of 15ft using the DAE-31 airfoil, a maximum takeoff weight (MTOW) of 35lbs, and a tail moment arm (TMA) of 90in. We will use a tractor propulsion configuration, a tricycle landing gear configuration, and a boom tail. The fuselage of the aircraft is a balsa semi-monocoque design surrounding an aluminum truss for strength. Our wings have a washout from 4.5° to 0○ and our tailplane is raised by 6in. Detailed descriptions of the design process are presented in Sec. 5

3.2 Optimization

Our configuration optimization process consisted of selecting an airfoil, designing a planform, and finally ensuring stability and control. This section discusses the first two steps, and design for stability and control can be found in Secs. 6.3 and 6.4.

3.2.1 Airfoil Selection

Because the objective of the competition is to carry as much payload as possible with a limited amount of power (and therefore thrust), we considered airfoils with a high ratio of lift coefficient to drag coefficient (C_L/C_D) for a large range of angles of attack α. This is because while in steady level flight, the thrust required is given by

$$T_{\text{req}} = \frac{W}{F_L/F_D} = \frac{W}{C_L/C_D} \tag{1}$$

where T_{req} is the required thrust, W is the weight of the vehicle, and F_L and F_D are the forces of lift and drag, respectively. Therefore, an increased C_L/C_D allows the same weight to be carried by a decreased thrust. After identifying several airfoils with high C_L/C_D using Airfoil Tools [3] for a large range of α, including the DAE-11, DAE-31, and AH 79-100 B, we decided to choose the DAE-31 airfoil. The reasoning for this decision was that, while the C_L/C_D ratios were similar among all four airfoils, we deemed the DAE-31 the most feasible to manufacture. Our wing construction strategy involves creating lightweight but strong hollowfoils by laser cutting balsa wood (see Sec. 8 for details); a few test cuts showed that the very thin trailing edges found on the DAE-11 and AH 79-100 B airfoils burned or snapped very easily, rendering any aerodynamic advantages obsolete.

3.2.2 Payload and Scoring Optimization

With the airfoil selected, our team turned our attention to planform design for scoring optimization. The competition scoring equation given by SAE Aero Design [1] is shown in Eqs. (2), where the goal is to maximize the Final Flight Score (FFS).

$$\begin{aligned} FFS &= FS_1 + FS_2 + FS_3 + WS \quad \text{, where} \\ FS &= \frac{W_{\text{payload}}}{2} + PPB \\ PPB &= \max\left(5 - \left(W_{\text{payload}} - P\right)^2, 0\right) \\ WS &= 2^{1+\frac{b}{5}} \end{aligned} \tag{2}$$

where each individual Flight Score (FS) incorporates the weight of the regular boxed cargo W_{payload} in pounds and the Payload Prediction Bonus (PPB), in which P represents the predicted payload, in pounds. The Wingspan Score (WS) uses the wingspan b of the aircraft, in feet. The top three Flight Scores are used in computation of the FFS. Importantly, the aircraft must take off within 100ft for the FS to be counted.

We decided therefore that it is important to develop a model for takeoff distance, noting that this analysis is conservative as thrust required for takeoff within 100ft would be greater than that required while cruising. By applying conservation of momentum, we developed the model shown in Eqs. 3-4 and verified it via various sources [2] [add more].

$$m\frac{\mathrm{d}v}{\mathrm{d}t} = T - \left(F_D + \mu_r\left(mg - F_L\right)\right) \tag{3}$$

where the weight W of the aircraft is given by mass times the acceleration due to gravity, mg, v is the ground velocity of the aircraft, T is the aircraft's thrust, F_D is the force of drag on the aircraft, F_L is the force of lift on the aircraft, and μ_r is the coefficient of friction (rolling resistance) between the tires and the ground. Integrating twice, we can solve for the takeoff distance x_{TO} by requiring that the takeoff speed has a 20% safety margin above the stall speed (a typical industry standard [2]):

$$x_{TO} = \frac{1.44W^2}{g\rho S C_{L,max}\left(T - \left(D + \mu_r(W - L)\right)\right)} \tag{4}$$

where the lift and drag L and D are evaluated at the average speed during takeoff roll, approximately $0.7v_{TO}$ [2].

Applying our constraint of approximately 45N of thrust T during takeoff (see Sec. 7 for details), we wrote a MATLAB script for takeoff analysis to determine the optimal wingspan b, planform area S, and payload weight W_{payload}. The reason these four variables are related and relevant to scoring is because the wingspan and planform area affect the overall lift L which can be generated by the aircraft as well as the aircraft's MTOW (greater b and S mean a heavier airframe!). Based on our model in Eq. (4), there exists a unique maximum total weight to achieve takeoff for any given T. This MTOW is a sum of W_{payload} and the weight of the airframe itself; we want to make W_{payload} as large a portion of the MTOW as possible to maximize our score, assuming our predicted payload matches our actual payload exactly.

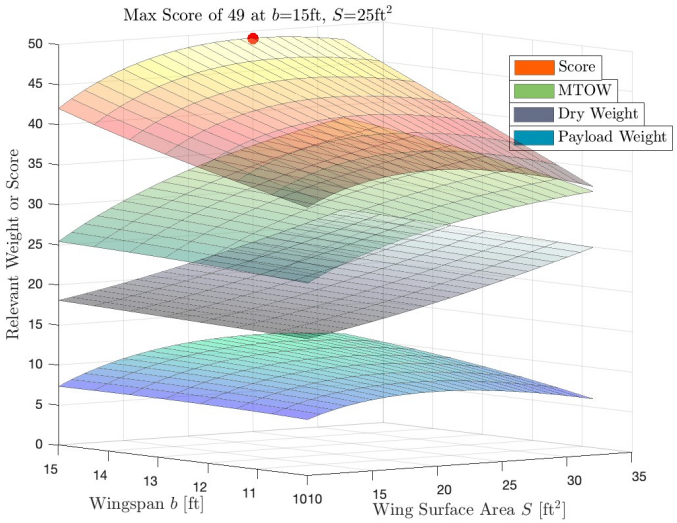


Figure 3: Score Optimization Plot (Score vs. Wingspan vs. Wing Area) for DAE-31 Airfoil

The results (Fig. 3) of our analysis showed that a wingspan of 15ft and area of about 25ft^2 would optimize our score (an aspect ratio $\mathcal{AR}$ of about 9). These results align with our intuition of designing for the maximum wingspan to maximize our score. Several important notes of the results:

1. As expected, increasing the wingspan and wing surface area increase MTOW.

2. An approximation of the dry weight of the aircraft was developed, which is proportional to the wingspan and to the logarithm of the surface area. This model was parameter-fitted based on our airframe weights from previous competition seasons.

3. Given a certain wingspan, there is a specific surface area which maximizes the payload carried (larger surface area increases the dry weight more than the MTOW).

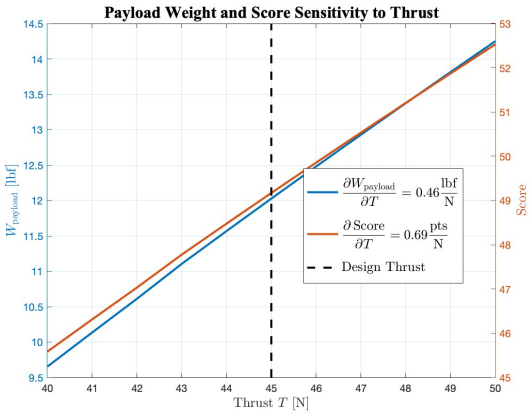
4. Although a similar W_{payload} may be achieved by various wingspans, the exponential wingspan score component in Eq. (2), the maximum wingspan still gives the maximum score.

We used our selected airfoil, wingspan, and aspect ratio to calculate the required payload vs. density altitude curve for our technical data sheet. By varying the density altitude and assuming an approximately constant available thrust, the total available lift varied linearly. This is because the lift generated is equal to $F_L = \frac{1}{2}\rho v^2 S C_L$, and varying the density altitude changes only ρ.

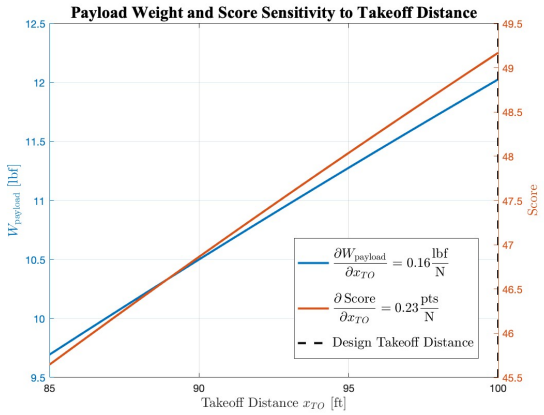
3.2.3 Design Sensitivities

In the above analysis, we made three key assumptions: (1) the available thrust is exactly 45N, (2) the coefficient of rolling friction μ_r is exactly 0.025, and (3) the takeoff distance is exactly 100ft. As we are relying on the analysis for configuration optimization, we decided that it is important to understand the sensitivity of our score to each of

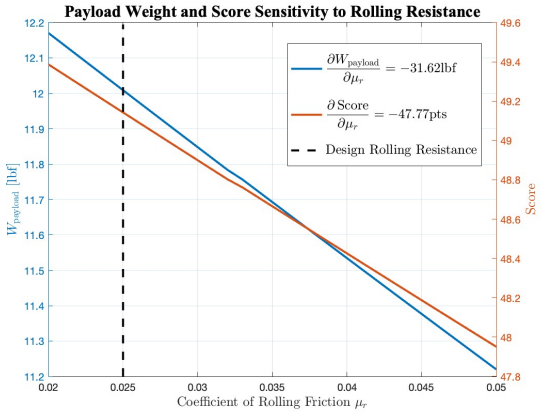
these parameters. Therefore, a MATLAB script was written using the same model in Eq. (4) to calculate the rate of change of W_{payload} and the score with respect to each of these parameters. The results are shown in Fig. 4.



(a) Thrust Sensitivity



(b) Takeoff Distance Sensitivity



(c) Rolling Resistance Sensitivity

Figure 4: Sensitivities of W_{payload} and Score to Fixed Parameters

The results align with intuitive expectations (greater thrust allows greater W_{payload}, shorter takeoff distance decreases W_{payload}, and increased μ_r decreases W_{payload}. More importantly, however, we notice that W_{payload} has an approximately linear relationship to all important parameters, indicating that we do not expect significant changes in performance due to slight modeling errors in any of these parameters.

4 Load Derivations and Assumptions

4.1 Aerodynamic Loads

The overall aerodynamic loads experienced by the aircraft are determined primarily by its equations of motion in its body-fixed coordinate frame [2], shown in Eqs. (5),

$$\begin{aligned} m\frac{\mathrm{d}v}{\mathrm{d}t} &= T\cos(\alpha - \alpha_T) - F_D - W\sin\gamma \\ m\frac{v^2}{r_c} &= F_L + T\sin(\alpha - \alpha_T) - W\cos\gamma \end{aligned} \tag{5}$$

where v is the airspeed of the vehicle, α is the absolute angle of attack, α_T is the angle of the thrust relative to the horizontal, γ is the angle of the flight path relative to the horizontal, and r_c is the radius of curvature of the flight path. T, F_D, F_L, m, and W are all defined as before (thrust, drag force, lift force, mass, and weight, respectively). In steady, level flight, Eqs. (5) simplify to

$$\begin{aligned} F_D &= T\cos\alpha \\ F_L &= W - T\sin\alpha \end{aligned} \tag{6}$$

which we will use for systems-level components such as the wing mount and fuselage. For more specific structures, such as the wing spars, wing ribs, empennage spars, empennage ribs, and boom tail, a more local lift and drag distribution will be required (i.e. spanwise or total). For these structures, we used the standard lift, drag, and moment equations

$$F_L = \frac{1}{2}\rho v^2 S C_L, \quad F_D = \frac{1}{2}\rho v^2 S C_D, \quad M_a = \frac{1}{2}\rho v^2 S c C_{M_a} \tag{7}$$

where M_a is the moment about an arbitrary point a, and C_L, C_D, and C_M are the three-dimensional coefficients of lift, drag, and moment (see Sec. 4.1.1 for details on 3-D drag considerations). We then validated these calculations and obtained distributions via computational fluid dynamics (CFD) simulations in XFLR5 (see Fig. 5).

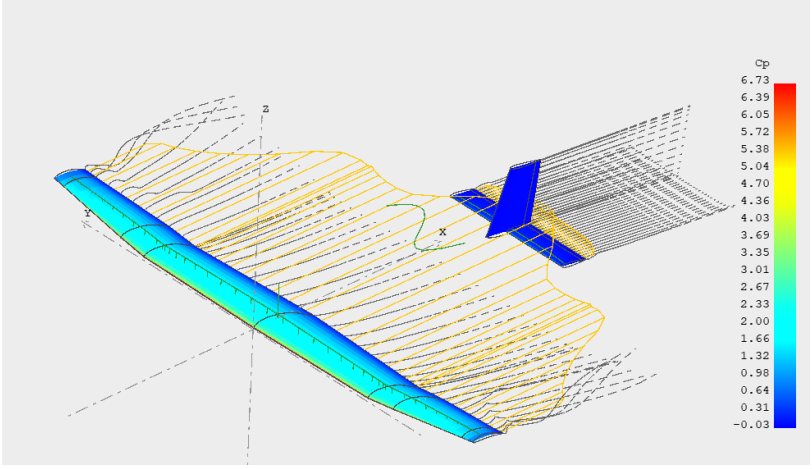


Figure 5: 3D Drag simulation in XFLR5

4.1.1 3-D Drag Considerations

To account for three dimensional drag effects, our team utilized both simulations and accepted analytical models [2]. We modeled three-dimensional lift using an aspect ratio correction and induced angle of attack

$$C_L = c_{l_{\alpha_0}} \left(1 + \frac{180}{\pi}\frac{c_{l_{\alpha_0}}}{\pi e_1 \mathcal{AR}}\right)^{-1} (\alpha - \alpha_{L=0}) \tag{8}$$

where $c_{l_{\alpha_0}}$ is the 2-D lift slope for the airfoil, e_1 is the span efficiency factor, $\mathcal{AR}$ is the aspect ratio, α is the angle of attack in degrees, and $\alpha_{L=0}$ is the zero lift angle of attack. Subsequently,

$$C_D = c_d\left(c_l\left(\alpha_{\text{eff}}\right)\right) + \frac{C_L^2}{\pi e_1 \mathcal{AR}} \tag{9}$$

where the effective angle of attack α_{eff} is given by

$$\alpha_{\text{eff}} = \alpha - \frac{180}{\pi}\frac{C_L}{\pi e_1 \mathcal{AR}} \tag{10}$$

Additionally, we verified the 3-D drag coefficients of our finite wing using the analysis XFLR5 analysis from Fig. 5.

4.2 Landing Loads

In order to estimate the dynamic landing loads experienced by the aircraft, our team modeled the aircraft's suspension system as a mass-spring-damper system, represented by the differential equation

$$m\ddot{x} + c\dot{x} + kx + F = 0 \tag{11}$$

where m is the mass of the aircraft, c is a damping constant, k is a spring constant, and F is an externally applied load. Based on this differential equation, our team developed a Simulink model to simulate various landing conditions, shown in Fig. 6.

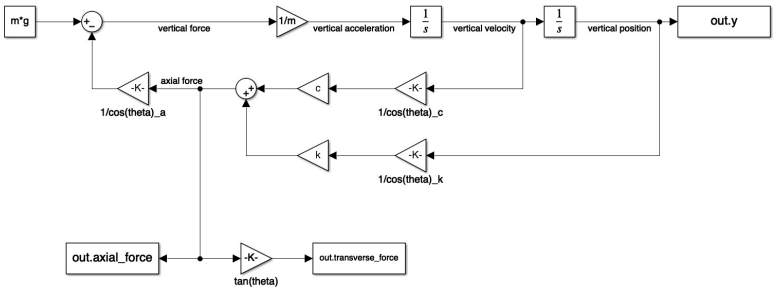


Figure 6: Simulink Model for Landing Loads

By applying an impulse load to simulate the landing load, and iterating over a variety of damping constants since we cannot reliably measure the damping constant of our full assembly, we determined a conservative impulse landing load of 85lbf. Then, conservatively assuming zero damping, we calculate the required effective spring constant for our aircraft to be $28\frac{\text{lbf}}{\text{in}}$.

5 Structural Design and Analysis

5.1 Component Loading and Design

Our team used a variety of techniques to design, size, and analyze the structural component of our aircraft. These ranged from hand calculations using classical statics and mechanics to finite element analysis (FEA). For convenience, Tab. 2 lists the minimum safety factors for critical structural components of our aircraft. The following section will detail the methods used to calculate these safety factors.

Table 2: Safety Factors of Critical Components

Component	Minimum Safety Factor (compared to normal operation)
Fuselage Semi-monocoque Structure	13.9
Trussed Wing Mount	25
Wing Spars	2.4
Fuselage-to-Tail Integration	3.3
Boom Tail	2.4
Landing Gears	

5.1.1 Classical Statics

Solid mechanics and statics were heavily utilized in the design of various components, including the longerons and bulkheads that comprise semi-monocoque fuselage, the boom tail, and the spars of aerodynamic surfaces. These components were modeled as either cantilevered or simply supported beams, depending on the boundary conditions, and appropriate loads were applied. For example, the analysis of the fuselage involved applying the overall loads discussed in Sec. 4, the tail was modeled as a cantilever with a point load due to stabilizer forces, and the wing spars utilized distributed local loads obtained by CFD, also as discussed in Sec. 4. In general, the total shear force V and moment generated M due to a set of loads $F(x)$ is calculated as

$$V(x) = \int F \, \mathrm{d}x, \quad M(x) = \int xF \, \mathrm{d}x \tag{12}$$

where the integral becomes a summation for non-continuous (point) loads. Then, using classical statics [4], the deflection y of the beam can be calculated as

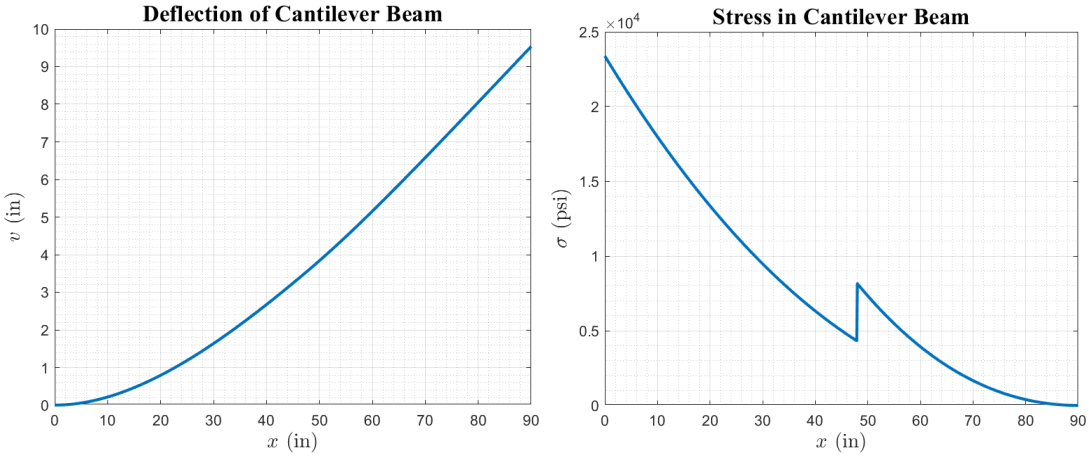
$$\frac{\mathrm{d}^2 y}{\mathrm{d}x^2} = \frac{M(x)}{E(x) I_{xx}(x)} \tag{13}$$

where $E(x)$ is the local Young's modulus and $I_{xx}(x)$ is the local second moment of area. In certain simplified cases, such as the isotropic material, constant cross-sectional area of the wing spar and boom tail, both E and I are constant as a function of x, simplifying the above equation. With the moment solved, it is also possible to determine the stress σ in the material as

$$\sigma = \frac{M(x)c}{I_{xx}} \tag{14}$$

where c is the distance from the neutral axis. Based on the material stress and deflection, we determine if each component yields or exceeds a critical deflection limit.

For many of our components, we verified our hand calculations by writing a numerical MATLAB script which numerically integrates to determine the moment, stress, and deflection. An example of the output of this script is shown in Fig. 7 (note that due to the spars being telescoping, the second moment of area decreases at 48 inches).



(a) Main Spar Deflection (b) Main Spar Stress

Figure 7: Example of Beam Analysis

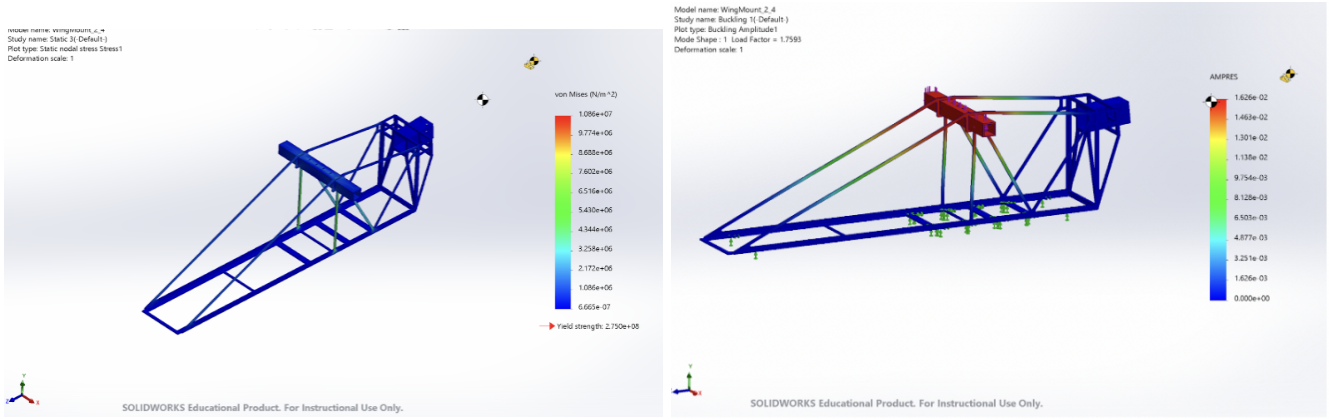
In addition to beam analyses, our team used the Euler buckling method to evaluate whether certain members, especially in the wing mount, would buckle. The critical Euler buckling load P_{crit} is given [4] as

$$P_{\text{crit}} = \frac{\pi^2 EI}{(KL)^2} \tag{15}$$

where the product KL is the effective length of a column [4].

A particularly unique analysis we conducted was the use of the method of joints in determining the loads in our trussed wing mount, which also supports the landing gears and boom tail. We decided to utilize a truss due to its efficiency in transferring large loads (such as landing and lifting loads) while maintaining a very low weight. Furthermore, using a truss for our wing mount offered high versatility to accommodate the geometry of our aircraft as needed.

5.1.2 Finite Element Analyses

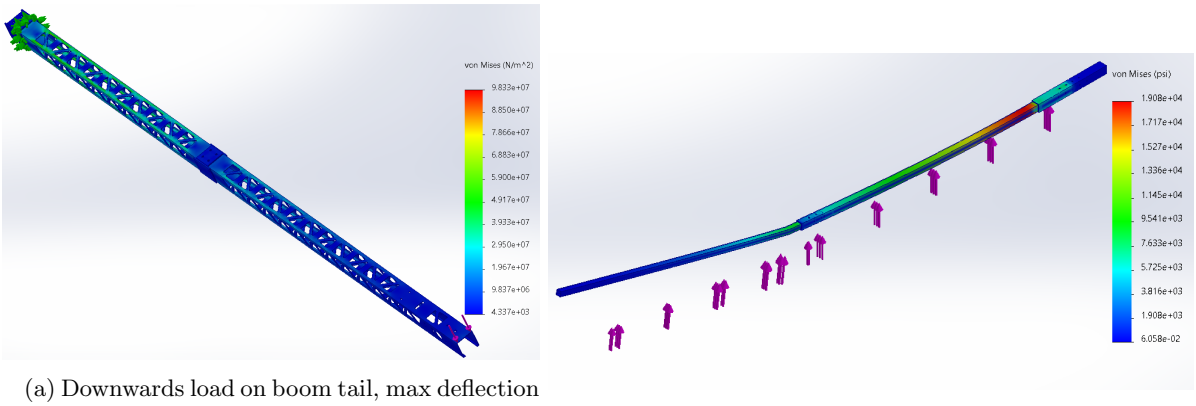


(a) Stress Analysis from Lifting Force (b) Truss Buckling Analysis

Figure 8: FEA of Wing Mount Truss

To validate our classical methods, we also conducted FEA to verify the survivability of different structures. For example, we ran extensive simulations on our wing mount under various loads and combinations of loads, ensuring that the material itself does not yield and that the truss as a whole does not buckle. The results of these simulations, shown in Fig. 8 validate the survivability of our design.

Similar analyses were also carried out on our trussed boom tail and telescoping wing spars. We selected a boom tail over a conventional tail mainly because of the modularity requirement. Last season, we used a conventional tail design with a cruciform supporting structure, which itself was structually sound, but made integration to the fuselage a large weak point. Analysis on last year's integration showed that there were very large notch stresses [5] at the integration point, which we decided to avoid this year via a fastened boom tail (see Sec. 5.3 for details). The FEA simulations on the boom tail focused primarily on stress and deflection, as these are the two most critical properties for the structural integrity of the tail and effectiveness of the empennage. Meanwhile, the FEA simulations on the wing spars prioritized stress, as from prior experience the Monokote covering of our wings significantly stiffens the assembly and reduces deflection.



(a) Downwards load on boom tail, max deflection of 1.23in.

(b) Distributed lift load on wing spar, max stress of 19kpsi

Figure 9: FEA of Boom Tail and Wing Spar

5.2 Landing Gear Configuration and Selection

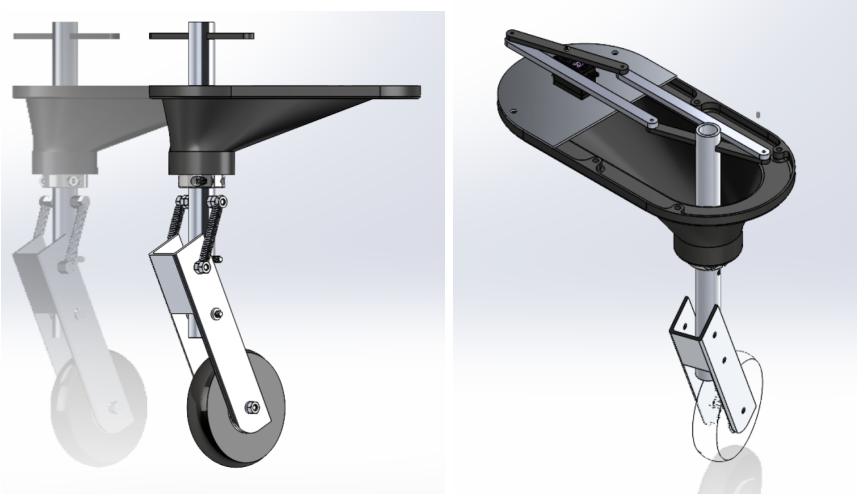
We opted for a conventional tricycle landing gear (LG) configuration with two wheels in the rear, and one wheel in the front. We compared the tricycle configuration to the taildragger configuration as it often is simpler and lighter. However, at low velocities, induced drag dominates, and the high angle of incidence during takeoff significantly increases the drag coefficient (around 0.09 for a taildragger vs only 0.02 for the tricycle configuration). Thus a taildragger reduces the amount of payload which can take off within 100ft. Because the competition ruleset dictates that we must take off in 100ft and are scored by payload carried, we conclude a tricycle configuration is more appropriate. Refering to [6], the required wheelbase (28.25in.) and rear wheeltrack (31.5in.) were calculated to ensure a turnover angle below 63° and so that the static load on the front LG is sufficiently small to allow for steering (below 7lbf). The resulting dimensions are shown in Tab. 3.

Table 3: Critical Landing Gear Dimensions

Wheelbase	Rear Wheeltrack	LG Height	Turnover Angle	Front LG Static Load
28.25in	31.5in	14.2in	46.9°	6.7lbf

5.2.1 Front Landing Gear

For the front landing gear (FLG), our team conducted a trade study comparing a new trailing link configuration common on commercial aircraft to the telescoping tube design we have used in the past. We compared both the overall weight of the landing gear as well as the force transmitted to the fuselage, relying on the Simulink model developed in Sec. 4.2. We found that with a 33% reduction in weight, the trailing link also reduces the force transmitted to the fuselage by 67%, a clear indication that we should use the trailing link design. Furthermore, we argue qualitatively that the trailing link allows greater flexibility during landing, accommodating variations in terrain and reducing the likelihood of structural damage. Our trailing link design is shown in Fig. 10a, and its corresponding push-pull steering mechanism is shown in Fig. 10b



(a) FLG Assembly (b) FLG with Steering Mechanism

Figure 10: FLG CAD

5.2.2 Rear Landing Gear

For our rear landing gear (RLG), research into materials was of particular interest. The last few seaons, we have explored both commercial carbon fiber gears as well as custom aluminum gears with mixed results. In the past, the structural integrity of the carbon fiber gears was brought into question due to high deflection, but the aluminum gears were much heavier. Our goal this year was to determine which option would be optimal.

Using topology optimization, we determined what type of design would be optimal if we used a custom aluminum landing gear, and these results are shown in Fig. 11

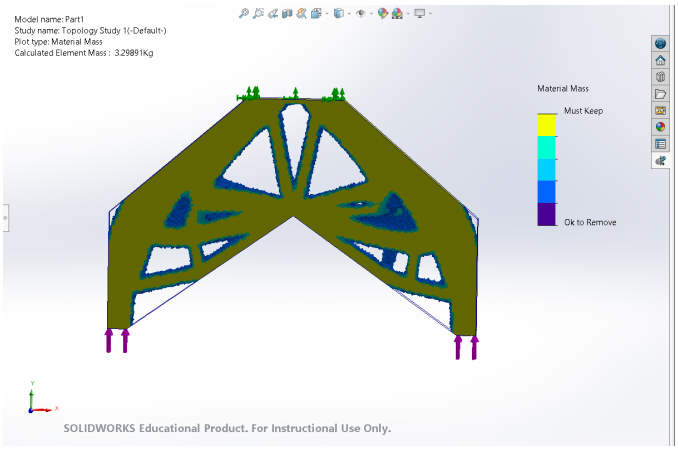


Figure 11: Topology Optimization for Aluminum RLG

Meanwhile, we performed drop testing on a previously owned commercial carbon fiber RLG to measure its deflection. The setup, shown in Fig. 12 involved both placing and dropping from approximately 2 feet increasing amounts of weight onto a single leg of the RLG, which was secured using metal brackets to a platform. The drops were recorded in slow motion and the deflections were measured, shown in Tab. 4



Figure 12: RLG Testing Setup

	Static Test		Drop Test	
	10lbf	30lbf	20lbf	30lbf
Deflection	0.28 in.	0.71 in.	5.25 in.	6.53 in.
Failure	No	No	No	Yes

Table 4: RLG Testing Deflections

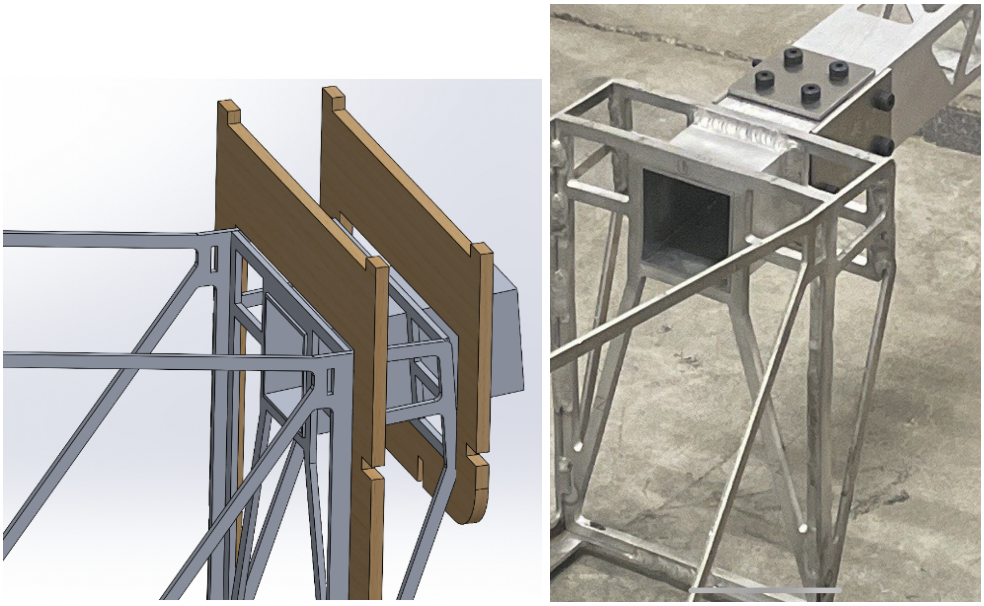
Based on these results, and in conjunction with the topology optimization of the aluminum RLG from above, we decided that a commercial carbon fiber RLG was more optimal. The carbon fiber landing gear tested was only about $\frac{1}{8}$in thick and was significantly smaller than the one we planned on purchasing for our final aircraft, and only failed when nearly the full weight of the aircraft was dropped on one leg. Therefore, we had faith that the larger, thicker RLG we planned on purchasing would be sufficiently strong for our aircraft. Additionally, it would be significantly lighter with a significantly lower frontal area (thus reducing drag) than the aluminum RLG.

5.3 Integration and Modularity Design

Per the competition rules, one important design constraint is the modularity requirement, in which no part can be greater than 48in. along a principal axis. Therefore, a large focus was put on designing structurally sound integration between components.

5.3.1 Tail to Fuselage Integration

Our decision for tail configuration were largely influenced by the modularity requirement. We conducted a trade study comparing conventional and boom tail designs, evaluating center of gravity position, weight calculations, and integration strength, and we decided to use a boom tail, integrating directly to the wing mount. We would add two vertical aluminum 6061 brackets on the wing mount to which the tail could be bolted, shown in Fig. 13a. Then, the boom tail itself could be bolted onto a square extension which was welded to these brackets, as shown in Fig. 13b.



(a) Tail Integration Modification on Wing Mount (b) Bolted Integration for Boom Tail

Figure 13: Tail Integration Design

Having performed an FEA analysis on this integration point, we found that the vertical brackets of the truss would require a thickness of $\frac{1}{4}$in due to the large cantilever moment.

5.3.2 Internal Tail Integration

Integration between the two tail sections was very similar to integration between the fuselage and the tail. A set of plates surrounded the two segments and shoulder bolts were used hold them together, with strengths verified via a shear analysis. Integration of the horizontal and vertical stabilizers entailed bolting the root ribs to the tube walls and gluing the spars into corresponding holes tail.

5.3.3 Spar Integration

Similar to the tail, the wing spars are held together via fasteners. However, they differ in that they are telescoping and therefore do not require the external plates seen on the tail, and that their integration point is in the internal volume of the wing. In order to allow for their assembly and disassembly, we make small cuts in the external Monokote so that we can access the fasteners. From our experience during competition last year, we know that the minor cutouts do not drastically influence the aerodynamic performance of the wing.

5.4 Weight and Balance

In order for an accurate estimation of our center of gravity (CG) as the plane was being designed, we utilized a weight and balance table over the duration of the design and manufacturing process. Since many of the design components rely on the CG and vice versa, the table had to be kept up while designs were being created and edited.

Table 5: Weight and Balance Table

Subsystem	Component	Weight (lbf)	x-position (in.)[a]	Resultant Moment (lbf $\cdot$ in.)
Electronics	Motor	1.4	-30.23	-43.32
Electronics	Receiver	0.2	-30	-6
Electronics	Battery	1.07	-29.11	-31.14
Fuselage	Overall Structure	4.4	1.93	8.49
Tail	Overall Structure	2.22	53.4	118.55
Landing Gear	Front	3	-21.98	-65.94
Landing Gear	Rear (Main)	1.7	6.27	10.65
Wing	Overall Structure	5.34	1.3	6.94
Empennage	Overall Structure	1.3	93	120.9
Fuselage	Ballast	1.5	-27	-40.5
Totals	-	22.1	-	67.97
Center of Gravity	-	-	3.07	-

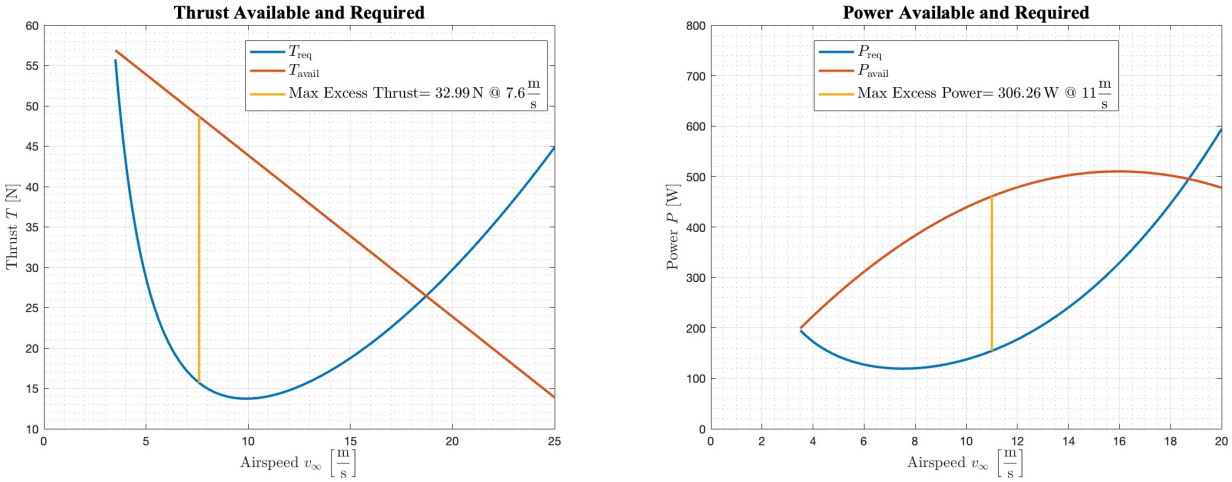
[a]Measured from the spar, positive in the aft direction

Based on the stability analysis discussed in Sec. 6.3, the maximum allowable x_{CG} is 5in., so our target x_{CG} was set to 3in. The designs targeted specific weights to achieve this x_{CG} and ballast could be used after manufacturing in case the actual x_{CG} differed from our target. As more components were manufactured, we weighed them in order to obtain a more accurate estimate of x_{CG}.

6 Aerodynamic Performance Analysis

6.1 Takeoff and Climb

A detailed takeoff analysis is discussed in the scoring Sec. 3.2.2, as our competitive performance is strongly dictated by our ability to take off in the required 100ft. To determine our maximum angle and rate of climb, we first find the maximum excess thrust and power, shown in Fig. 14.



(a) Maximum Excess Thrust

(b) Maximum Excess Power

Figure 14: Climb Analysis

From these results, and assuming steady flight, we can calculate [2] our vehicle's maximum climb angle $\gamma_{\max}$ as

$$\gamma_{\max} = \arcsin\left(\frac{\text{Maximum Excess Thrust}}{W}\right) = 13.34^\circ \tag{16}$$

and our vehicle's maximum rate of climb $\dot{y}_{\max}$ to be

$$\dot{y}_{\max} = \frac{\text{Maximum Excess Power}}{W} = 1.96\frac{\text{m}}{\text{s}} = 6.48\frac{\text{ft}}{\text{s}} \tag{17}$$

6.2 Lifting and Cruise Performance

A V-n diagram for our vehicle is shown in Fig. 15, giving the stall and corner speeds for our aircraft ($9.6\frac{\text{m}}{\text{s}}$ and $15\frac{\text{m}}{\text{s}}$ respectively) as well as the overall load factor limits of -2 and $+2.4$ based on the structural designs in Sec. 5.

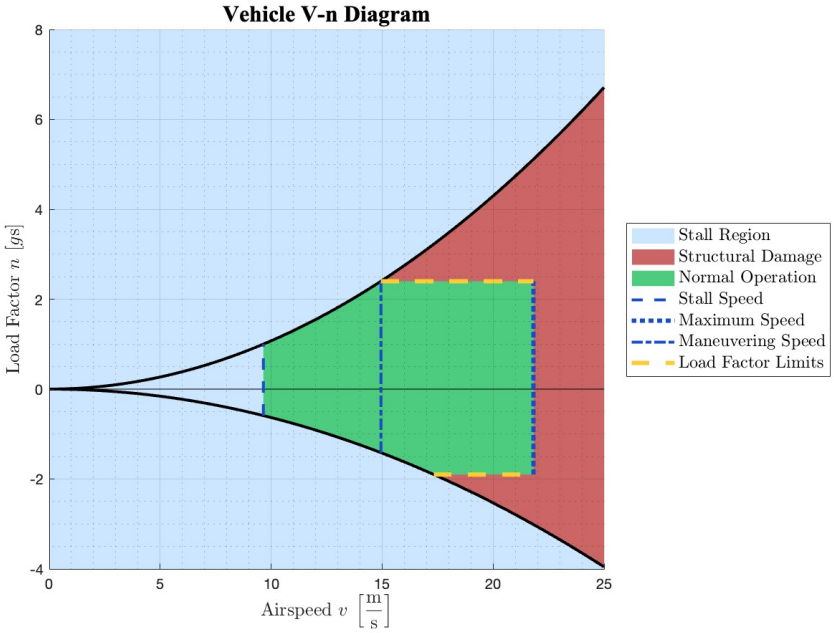


Figure 15: V-n Diagram for Vehicle

6.3 Stability

6.3.1 Horizontal Stabilizer

Our main goals for our horizontal stabilizers (H-stabs) were to reduce both the weight and size of our horizontal stabilizers. We received feedback from our pilot last year that our stabilizers were too big for the size of our aircraft and experienced a lot of trouble with the modularity requirement with regards to our H-Stab and therefore decided to reevaluate our method for sizing the H-stab, aiming for a maximum span of 48in.

Yet another design flaw in our aircraft last year was our lack of consideration of its CG. Our CG last year was too close to our neutral point which, coupled with low thrust, caused difficulty taking off. Therefore, we took a CG approach to sizing our H-Stab and then used that sizing to determine a maximum distance behind the spar for the CG. For static stability, the following requirements hold [2]:

$$\begin{aligned} C_{M_0} = C_{M_{AC},wb} + C_{L_{\alpha_{wb}}}\alpha_{wb}(h - h_{ac,wb}) - V_H C_{L_{\alpha_t}}\alpha_{wb} + C_{L_{\alpha_t}} V_H(i_t + \epsilon_0) > 0 \\ \frac{\partial C_{M,cg}}{\partial \alpha_a} = C_{L_\alpha}(h - h_{ac,wb}) - V_H C_{L_{\alpha_t}} < 0 \end{aligned} \tag{18}$$

where V_H is the tail volume coefficient, $C_{M_{AC},wb}$ is the zero lift moment coefficient of the wing and body, $C_{L_{\alpha_{wb}}}$ is the lift slope of the wing and body, α_{wb} is the angle of attack of the wing and body, $(h - h_{ac,wb})$ is the distance from the CG to the aerodynamic center, $C_{L_{\alpha_t}}$ is the lift slope of the H-stab, i_t is the tail setting angle, and ϵ_0 is the downwash angle. Using Eqs. (18), we used Matlab to iterate through different CG locations noted in the equations as $(h - h_{ac,wb})$ to determine a range of allowable V_H, which was then used to solve for an H-stab area. We decided on a CG point that was a maximum of 5 inches behind the spar and an horizontal stabilizer area of 465in^2, giving us a tail volume coefficient of 0.65 and a positive static margin of 0.40.

6.3.2 Vertical Stabilizer

The vertical stabilizer (V-stab) maintains the yaw stability of the aircraft. Because we want the plane to be equally stable in either yaw direction, we chose the symmetric NACA 0015 airfoil, which also has a high stall angle.

We can calculate the yaw moment contributions of the wing and fuselage to find the moment that the V-stab needs to counteract to stabilize the plane and by extension S_v using these equations from [11]:

$$\begin{aligned} C_{n_{\beta_w}} &= C_L^2\left(\frac{1}{4\pi \text{Æ}} - \left(\frac{\tan\lambda}{\pi \text{Æ}(\text{Æ} + 4\cos\lambda)}\right)\left(\cos\lambda - \frac{\text{Æ}}{2} - \frac{\text{Æ}^2}{8\cos\lambda} + \frac{6(h_{acw} - h_{cg})\sin\lambda}{\text{Æ}}\right)\right) \\ C_{n_{\beta_{\text{fus}}}} &= -1.3\frac{V_f}{S_w b}\left(\frac{D_f}{w_f}\right) \\ C_{n_{\beta_v}} &= C_{F_{\beta_v}}\frac{\partial \beta_v}{\partial \beta}\eta_v\frac{S_v}{S_w}(l_t) \\ C_{n_\beta} &= C_{n_{\beta w}} + C_{n_{\beta_{\text{fus}}}} + C_{n_{\beta_v}} \end{aligned} \tag{19}$$

where $C_{n_{\beta_w}}$, $C_{n_{\beta_{\text{fus}}}}$, and $C_{n_{\beta_v}}$ are the yaw moment contributions of the wing, fuselage, and V-stab respectively, C_L is the coefficient of lift of the wing, λ is the sweep angle of the wing, Æ is the aspect ratio, $(h_{acw} - h_{cg})$ is the distance between the aerodynamic center of the wing and the plane's center of gravity, w_f is the width of the fuselage, V_f is volume of the fuselage, D_f is the depth of the fuselage. $\frac{\partial \beta_v}{\partial \beta}\eta_v$ is the lateral directional derivative which is calculated

from empirical data, $C_{F_{\beta_v}}$ is the derivative of the coefficient of lift of the V-stab at sideslip angle, and l_t is the tail moment arm, and C_{n_β} is the total moment needed to be produced by the wing, fuse, and V-stab. We assume C_{n_β} is a recommended value of 0.05 [11]. By rearranging Eqs. (19) we find $S_v = 320\text{in}^2$ which agrees with recommended values of $\frac{S_v}{S_w}$ between 0.09 – 0.10from [10].

Next we needed to determine the span of the V-stab which are affected by three parameters: The aspect ratio, taper ratio, and sweep angle. Each of these parameters have positive and negative effects on the stability of the plane. For instance increasing the sweep angle of the vertical tail causes the yawing moment arm to increase (improves directional control) and can also help decrease drag [10], but this can also weaken directional stability since the mass moment inertia about the z-axis is increased. Much of stabilizer design is about compromises between the effects of these parameters. Given these considerations, we determined the V-stab to have the following planform design:

Table 6: Vertical Stabilizer Features and Sizing

Span [in]	Root Chord [in]	Taper Ratio	Sweep Angle [deg]
21.17	17.60	0.7	14.01

6.3.3 Dynamic Stability Modes

Through XFLR5 simulations, we determined the times to halve and double amplitudes of dynamic stability modes and compared them to commonly acceptable values [7]. With our chosen wing planform and stabilizer design, our phugoid mode has a time to double amplitude of 36.6 seconds, which, considering a flight of not much longer than a minute, is sufficiently long. Our dutch roll mode has a relatively short time to half amplitude of 4.23 seconds, suggesting that our vertical stabilizer is sufficiently large to maintain yaw equilibrium. However, our spiral mode showed a relatively short time to double, being only 2.6 seconds. Therefore, we decided to implement a high wing as well as a dihedral to reduce instability in the spiral mode.

Our dihedral was implemented in a unique manner, taking advantage of the modularity requirement and mounting the wing tip sections at a dihedral angle relative to the root wing sections. This helps to increase spiral stability while not sacrificing too much lift at the root of the wing. To decide on the dihedral angle, we referred to [8] to determine an effective dihedral angle (EDA) as

$$\text{EDA} = \frac{5bc_l}{l_t} \tag{20}$$

where notably c_l is the lift coefficient of the *infinite* wing, b is the wingspan, and l_t is the TMA. For our aircraft, we calculate a required EDA of 12.25°, of which the implemented high wing accounts for approximately 5° [9]. Therefore, we implement an actual dihedral angle of 7.25°. with these changes, our new time to double in the spiral stability mode is 5.8 seconds, which we deem to be much more appropriate than the prior 2.6 seconds.

6.4 Control and Maneuverability

6.4.1 Elevators and Rudder

The elevators and rudder must be able to deflect to cause an equilibrium state for moments produced by the aircraft under certain conditions, such as when the aircraft is initiating a maneuver or when there is crosswind.

For the sake of manufacturing and simplifying our calculations, we decided that the each control surface (elevator and rudder) would be a rectangular planform spanning the entire length of the corresponding stabilizer at a percentage of the root chord. Another initial design decision was to limit the deflection of the control surfaces to 30 degrees in both directions as any more deflection could reduce effectiveness [10].

To find the moment that the each control surface needs to generate to perform its purpose, we used this equation[10]:

$$C_{M_\delta} = \frac{\partial C_M}{\partial \delta} \tag{21}$$

which essentially describes the fact that control surface effectiveness is mainly measured by the rate of change of the pitching or yawing moment (C_M) with the change in surface deflection angle (δ). Then,

$$C_{M\delta} = -C_{L_\alpha} V_t \eta \tau \frac{b_{cs}}{b_s} \tag{22}$$

where C_{L_α} is the lift curve slope, η is the dynamic pressure ratio ($\frac{q}{q_\infty}$), τ is the control surface effectiveness parameter, and V_t is the tail volume coefficient given by (TMA)$S_t S_w b_w$. τ_r can be found from Fig. 16 [10] which relates the control surface effectiveness parameter to the control surface chord to the lifting surface chord.

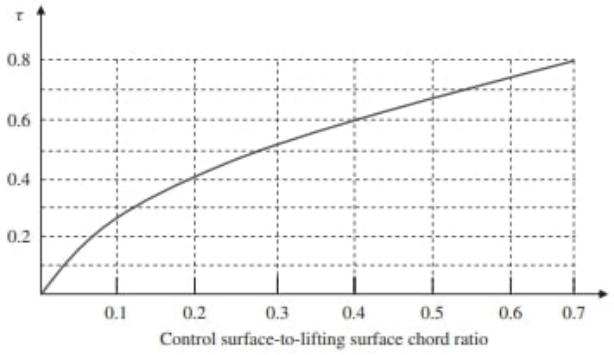


Figure 16: Effectiveness Parameter Graph

Because we set the span of the control surfaces and stabilizers to be the same, the only unknown in Eq. (22) is τ, which we can solve for. We can then reference the value we get with Fig. 16 to get the ratio of control surface chord length to stabilizer chord length. Based on these methods, we determined that the elevators would have a chord length equal to 0.25 times the chord length of H-stab and that the rudder would have a chord length equal to 0.20 times the chord length of the V-stab.

6.4.2 Ailerons

The dimensions, angle of deflection of the aileron, as well as the aircraft's bank angle were based on relevant equations for the corresponding class and size of the plane. Based on the class of our plane, we require a maximum roll time of 1.3 seconds to reach a bank angle of 30 degrees. [10]

Sadraey gives a general range for the dimensions of the ailerons' planform area ratio, chord ratio, and wingspan ratio [10]. Based on this source, the outboard of the aileron was placed at 0.95 of the semispan in order to maintain a powerful moment on the plane, but not too close to the wingtip to cause flow separation. The inboard of the wing was 0.65 of the semispan. The chord ratio of the plane was set to 0.25 of the wing chord.

The rolling of the plane based on its dimensions can be divided into two separate parts, the transient state roll and the steady state roll. The transient roll refers to the initial angular acceleration of the aircraft's roll that lasts until a given angle ϕ_1. After ϕ_1, the aircraft's roll then becomes constant, known as steady state roll. The steady state roll rate P_{ss} can be calculated by this equation

$$P_{ss} = \sqrt{\frac{2L_A}{\rho(S_w + S_h + S_{vt})C_D y_D^3}} \tag{23}$$

Where S_w is the wing surface area, S_h is the horizontal stabilizer area, S_{vt} is the vertical stabilizer area, C_D is the coefficient of drag, ρ is the air density, and y_D is the distance from the the roll axis of the aircraft to the center of drag. Furthermore, L_A is given by

$$L_A = \frac{1}{2}\rho(qy_D)^2(S_w + S_h + S_{vt})C_D y_D \tag{24}$$

Where q is the dynamic pressure. The angle at which transient roll stops is given by

$$\phi_1 = \frac{I_{xx}}{\rho y_D^3(S_w + S_h + S_{vt})C_{D_R}} \ln(P_{ss}^2) \tag{25}$$

and the angular acceleration is given by

$$\dot{P} = \frac{P_{ss}^2}{2\phi_1} \tag{26}$$

Where I_{xx} is the moment of inertia of the plane which we calculated using the SolidWorks mass properties tool based off of our aircraft CAD. The time to reach the 30 degree requirement ϕ_{des} is calculated by adding the period of the steady state roll and transient roll:

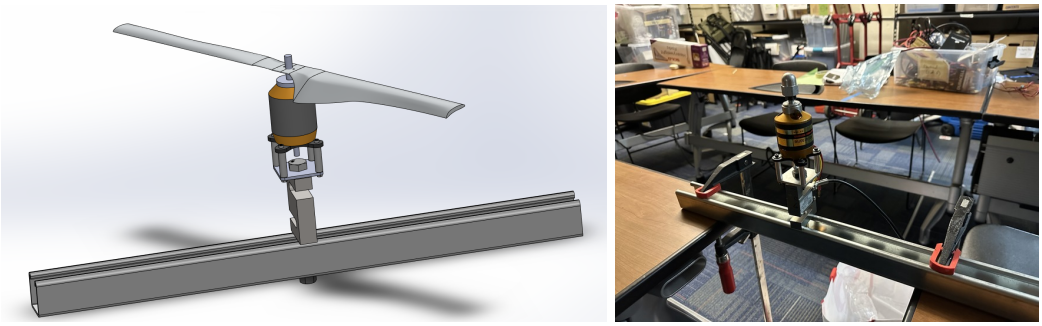
$$t = \sqrt{\frac{2\phi_1}{\dot{P}}} + \sqrt{\frac{2\phi_{des}}{\dot{P}}} \tag{27}$$

At full deflection, the total time to roll our aircraft to 30 degrees is 0.54s, meeting the 1.3s requirement for the plane to safely roll.

7 Propulsion and Testing

In previous years, we have attempted to develop several analytical models for dynamic thrust based on propeller diameter, pitch, and angular velocity. However, these attempts were not successful, as evidenced by our failed takeoff

last year. Therefore, our team this year decided to conduct several static thrust tests to calibrate an empirical model, and then use online propeller calculators to estimate dynamic thrust. We measured the thrust produced by various combinations of motors and propellers the team owned previously, using the setup shown in Fig. 17. The results are shown in Tab. 7.



(a) CAD of static thrust testing stand (b) Assembled thrust testing stand

Figure 17: Static Thrust Testing Setup

Table 7: Thrust in Newtons for Various Motor/Propeller Combinations

Motor (Kv)	Propeller		
	20in × 9in	24in × 5in	27in × 13in
Spektrum Avian 6362 (200)	31.47	34.62	32.07
AXI Gold Line 4130/16 (385)	37.20	45.60	50.57

As the 27in × 13in propeller with the AXI Gold Line 4130/16 motor produced the most thrust, we selected this combination for our final vehicle.

For dynamic thrust, we calibrated these values against a hybrid model that combined experimental data and the actuator disc model [12]; then, we verified the trends using other calculators such as eCalc [13] and E-Props [14]. The results are shown in Fig. 18.

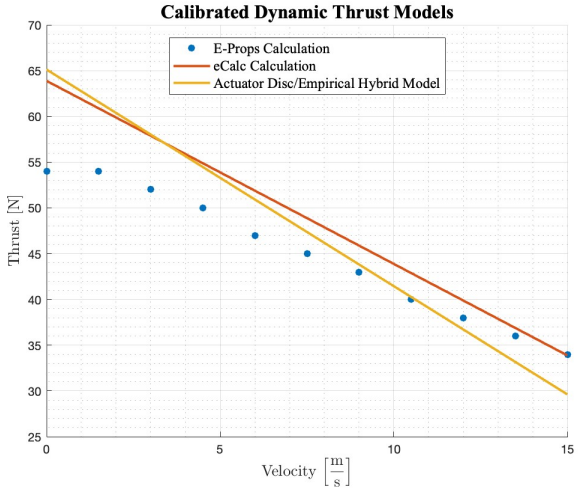


Figure 18: Calibrated Dynamic Thrust Models

From the models in Fig. 18, we concluded that during a takeoff roll in which the vehicle reaches our takeoff speed of $9.5\frac{\text{m}}{\text{s}}$, our vehicle's dynamic thrust would not average below 45N, a constraint we used when optimizing our score, payload, and wingspan design in Sec. 3.2.2.

8 Materials and Manufacturing

8.1 Material Selection

Our vehicle is constructed primarily of balsa wood and aluminum. We compared the strength-to-weight ratio of various wood types, including balsa, spruce, and birch. Specifically, we compared the weights of these wood types that would provide sufficient safety margins given our derived loads, as detailed in Sec. 5. In most cases (i.e. for the fuselage construction, wings ribs, and empennage ribs), balsa wood proved to be the most effective, as we could glue multiple layers of balsa together with grains in perpendicular directions. This essentially formed a laminate of very lightweight but sufficiently strong material. Spruce and birch wood also showed some promise, but we decided it was not worth the manufacturing difficulties and cost associated with using extremely thin spruce or birch. Using slightly thicker spruce or birch, on the other hand, would simply increase the overall airframe weight and forgo any weight savings.

The specific components for which spruce wood proved necessary were the spars for the horizontal and vertical stabilizers, as well as the integration points between the stabilizers and tail. The main reason for the use of spruce in these components was due to bending stresses higher than the strength of balsa. From sampling some leftover balsa scraps, we found that the bending strength of balsa wood was below 1MPa, while we expect stresses at the integration point and in the spars of the empennage upwards of 3MPa. Upon testing spruce wood and validating our results against [15], we found that spruce has a rupture stress of 20MPa, giving a more acceptable safety factor above 6.

Finally, the components of our aircraft which will experience the highest loads, such as our wing mount truss and the wing spars, were manufactured using aluminum, primarily 6061 T-6 alloy. We selected this material for its high strength-to-weight ratio and ease of machining. We briefly explored the possibility of using other lightweight materials, such as 3D printed plastics with low infill density, but this manufacturing technique proved ineffective as the finished parts were especially weak along layer lines; the actual material properties were therefore unreliable. For certain subcomponents, such as the trailing link of the front landing gear, we chose aluminum 3003 for its ease of bending.

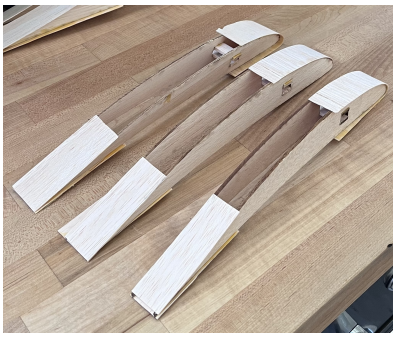
8.2 Manufacturing Technique Highlights

Most components of our aircraft are manufactured by laser cutting the aforementioned wood types, and then using wood glue to create a polymeric bond between parts. Aluminum components of our aircraft, such as the wing mount and landing gear, were cut using a water jet or FabLight laser, and then machined on a lathe or mill if necessary.

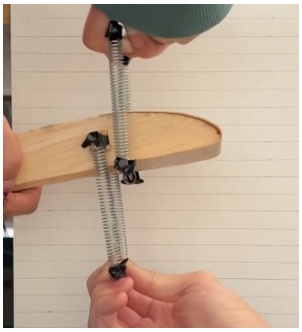
However, a few components of our aircraft feature unique manufacturing techniques which we highlight below.

8.2.1 Hollowfoils

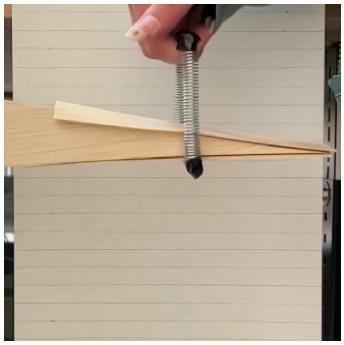
First, our wings feature a unique hollowfoil design (see Fig. 19a). This consists of two relatively thin airfoil profiles (ribs) joined by an outer skin to provide buckling and bending resistance.



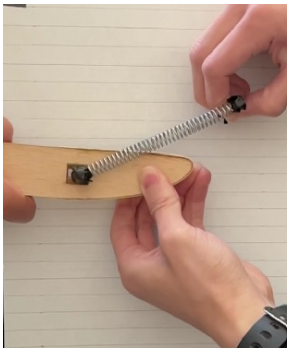
(a) Hollowfoil design



(b) Testing orientation 1



(c) Testing orientation 2



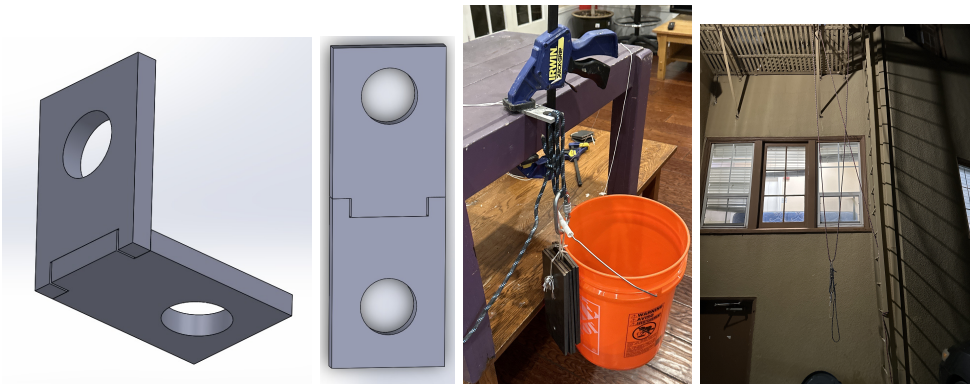
(d) Testing orientation 3

Figure 19: Hollowfoils and Testing

Hollowfoils with rib thicknesses of $\frac{1}{16}$in, $\frac{3}{32}$in, and $\frac{1}{8}$in were tested in three different loading conditions, shown in Figs. 19b-19d. All three thicknesses withstood a load of 6.86lbf in orientations 1 and 3, and the $\frac{3}{32}$in thick hollowfoil withstood a moment of $167\text{lbf}\cdot\text{in}$. We expect each hollowfoil to experience loads in the 1 and 3 orientations of around 2.9lbf and a moment in the 2 orientation of around $20\text{lbf}\cdot\text{in}$, giving us a minimum safety factor of 2.42. However, during the process of manufacturing these hollowfoils, we decided that the gluing process for $\frac{3}{32}$in hollowfoils was too inconsistent at the larger root foils, and that $\frac{1}{16}$in hollowfoils were too inconsistent altogether. Therefore, we concluded on using $\frac{1}{8}$in ribs for the center sections of the wings and $\frac{3}{32}$in ribs for the tip sections.

8.2.2 Wing Mount and Welds/Cold Welds

In previous seasons in which we used aluminum wing mounts, we have welded parts together. However, we struggled with significant undesired thermal warping after the welds cooled due to differential cooling and aluminum's high thermal expansion coefficient. Therefore, we decided to experiment with cold weld adhesives and test their shear strength as an alternative to welding. We considered two types of adhesive: Loctite and JB Weld, both of which are cold weld epoxies. To test their shear strength, we water jet cut several small samples of aluminum 6061 T-6, the exact alloy we planned to use for the wing mount, then we glued them together in both "planar" and "angular" configurations, shown in Figs. 20a-20b. For each adhesive/configuration combination, we clamped the configuration to a table and hung weight from it, (shown Fig. 20c). Soon, however, we surpassed the load for which the clamps were rated and instead used ropes to hang greater weights from the ceiling. Each configuration was loaded for a full minute at each weight increment to ensure that creep, strain softening, and fatigue were accounted for.



(a) Angular (b) Planar (c) Clamped Setup (d) Roped Setup

Figure 20: Cold Weld Epoxy Testing

The results are shown below in Tab. 8. Based on the results, we decided that JB Weld would be our adhesive of choice as it did not fail in the planar configuration and had greater shear strength in the angular configuration. Furthermore, the high loads sustained by the adhesive are sufficient to survive the loads we expect on the wing mount. Thus, we could avoid the risk of thermal warping due to actual welding by replacing necessary connections in the wing mount with JB Weld.

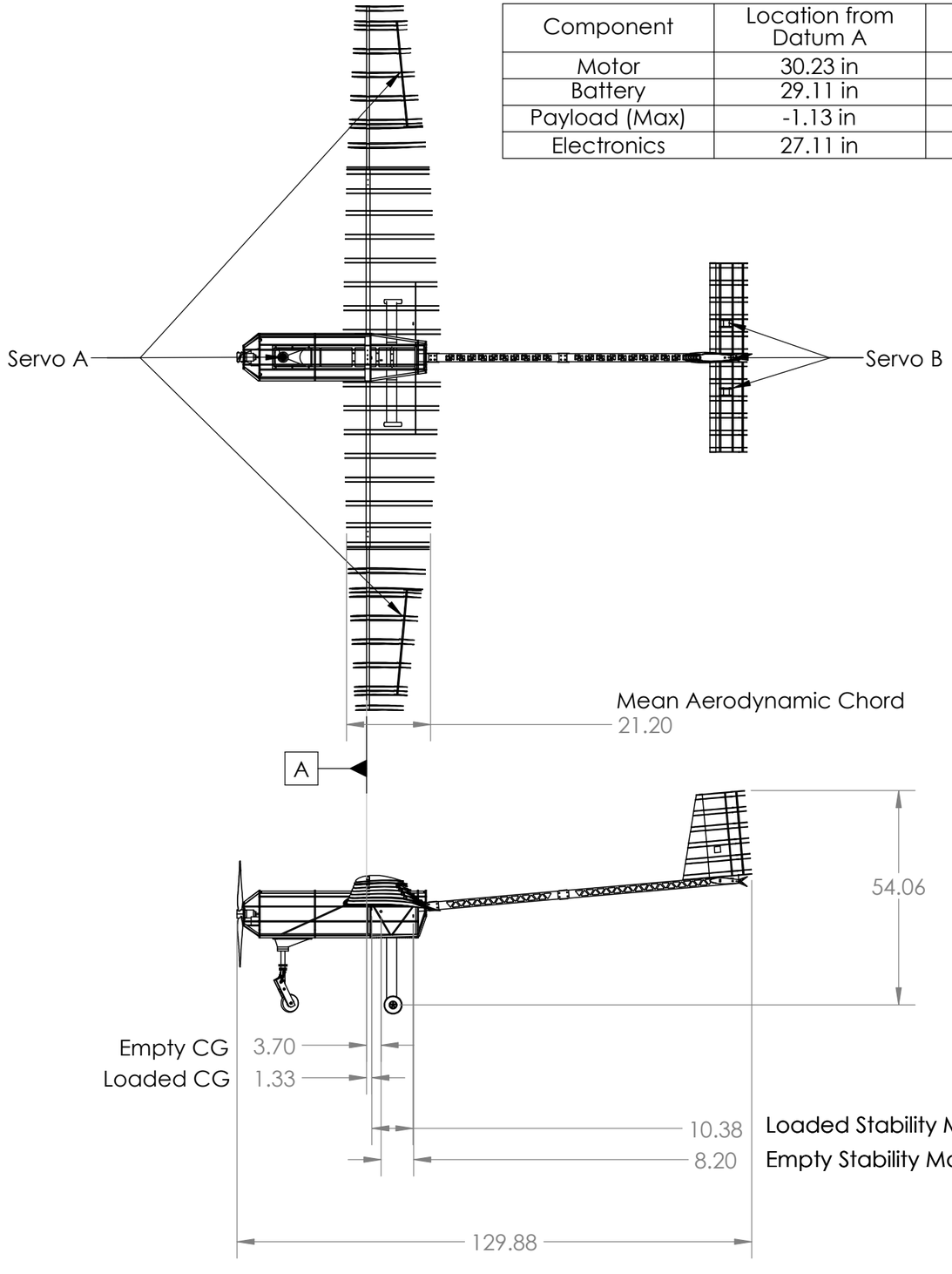
Table 8: Cold Weld Adhesive Testing Results

	JB Weld		Loctite	
Configuration	Planar	Angular	Planar	Angular
Weight Tested (lbf)	180	75	180	40
Failed?	No	Yes	No	Yes (Creep)

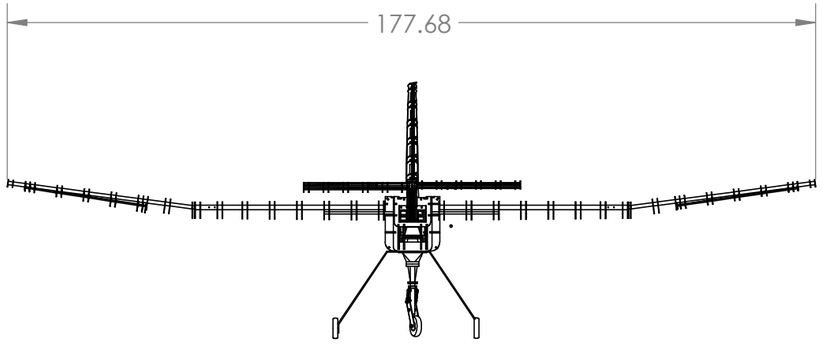
9 Conclusion

In conclusion, our team this year utilized a combination of analytical, software, and experimental methods to design and build an aircraft that we believe is competitive in the SAE Aero Design West competition. Where possible, we first developed analytical models for flight performance and structural integrity, and when these methods fell short, we implemented empirical methods or simulations. Furthermore, we also designed our aircraft in a way to minimize the risk of a catastrophic crash similar to that which we experienced last year. Instead, we modified our systems-level approach to the competition to first ensure a minimal scoring but successful flight, before slowly increasing our payload up to our maximum predicted payload. We believe that this approach will secure us several competitive scoring flights during the competition.

Component	Location from Datum A	Weight	Moment
Motor	30.23 in	1.4 lbs	43.32 lbf*in
Battery	29.11 in	1.07 lbs	31.15 lbf*in
Payload (Max)	-1.13 in	12.8 lbs	-14.46 lf*in
Electronics	27.11 in	.018 lbs	.488 lbf*in



Wingspan	177.68 in.
Wing Area	3542.4 in. sq.
Aspect Ratio	9.13
Empty Weight	22.6 lbs
Battery Capacity	3300 mAh
Motor	Axi Gold Line 4130/16
Motor KV	385 RPM/V
Propeller	APC Propellers, 27in x 13in
Servo A (Landing Gear, Ailerons)	Tower Pro MG9964 DIGI Hi-Torque, 152.76 oz-in
Servo B (Elevators and Rudders)	K-Power DMC911, 91 oz-in



UNLESS OTHERWISE SPECIFIED:

DIMENSIONS ARE IN INCHES
TOLERANCES:

TWO PLACE DECIMAL ± .25
THREE PLACE DECIMAL ± .05

INTERPRET GEOMETRIC TOLERANCING PER: ASME Y14.5

MATERIAL

FINISH

DO NOT SCALE DRAWING

University of California, Berkeley
Cal Aero SAE
Team 015

SIZE	DWG. NO.	REV
B	Final Plane Assembly	1

SCALE: 1:33.3 | WEIGHT: 22.6 lbs | SHEET 1 OF 1

Table of Acronyms

CAD - Computer Aided Design
MTOW - Maximum Takeoff Weight
TMA - Tail Moment Arm
AR - Aspect Ratio
CFD - Computational Fluid Dynamics
FEA - Finite Element Analysis
LG - Landing Gear
FLG - Front Landing Gear
RLG - Rear Landing Gear
CG - Center of Gravity
H-stab - Horizontal Stabilizer
V-stab - Vertical Stabilizer
EDA - Effective Dihedral Angle

References

[1] SAE International. "2024 Collegiate Design Series: SAE Aero Design Rules." SAE, 2024.

[2] Anderson, J. D. "Introduction to Flight," 8th ed. McGraw-Hill Education, 2016.

[3] "Airfoil Tools." Available at http://airfoiltools.com

[4] Beer, F., DeWolf, T., Johnston, E. & Mazurek, D. "Statics and mechanics of materials." McGraw-Hill Education, 2007.

[5] Mattheck, C., Wissner, C., Tesari, I., & Bethge, K. "Easing Cracks with the Method of Tensile Triangles." WIT Transactions on Ecology and the Environment, Vol. 138, 2010.

[6] Currey, N. S. "Aircraft Landing Gear Design: Principles and Practices." American Institute of Aeronautics and Astronautics, Inc., 1988.

[7] Stengel, Robert. "Flying Qualities Criteria." Princeton University, 2018.

[8] Beron-Rawdon, B. K. "Equivalent Dihedral Angle." RC-Soar, 1999. Available at https://www.rc-soar.com/tech/spiral_eda.htm

[9] Federal Aviation Administration. "Pilot's Handbook of Aeronautical Knowledge." U.S. Department of Transportation, 2023 here

[10] M. H. Sadraey. Aircraft Design: A Systems Engineering Approach. Wiley, West Sussex, United Kingdom, 2013.

[11] D. P. Raymer. Aircraft Design: A Conceptual Approach. American Institute of Aeronautics and Astronautics (AIAA), Blacksburg, Virginia, 6th edition, 2018.

[12] Staples, G. "Propeller Static & Dynamic Thrust Calculation." FliteTest, 2013. Available at https://www.flitetest.com/articles/propeller-static-dynamic-thrust-calculation.

[13] eCalc. Available at https://www.ecalc.ch.

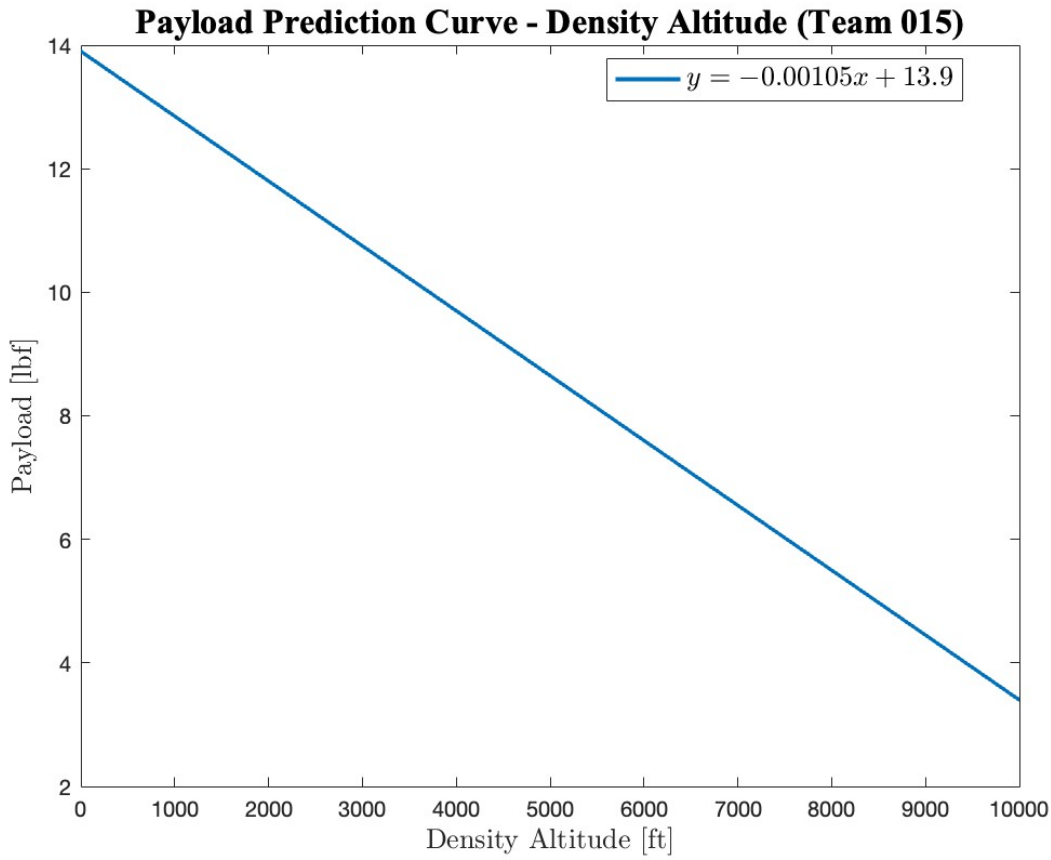
[14] E-Props. Available at https://www.e-props.fr

[15] Green, D., Kretschmann, D. & Winnandy, J. "Mechanical properties of wood." U.S. Department of Agriculture, Forest Service, Forest Products Laboratory, 1999.

[16] The Engineering ToolBox. "U.S. Standard Atmosphere vs. Altitude." The Engineering ToolBox, 2003. Available at https://www.engineeringtoolbox.com/standard-atmosphere-d_604.html.

[17] Bruhn, E. F. Analysis and Design of Flight Vehicle Structures. Tri-State Offset Co., 1973.

Technical Data Sheet - Payload Prediction



Technical Data Sheet for Team 015 (Cal Aero SAE). Refer to Section 3.2.2 for a full description of determination of the curve